Implantable, Biointegrated Optoelectronic Platforms with Ultrathin Encapsulation Layers as Long-Term Neural Interfaces

Xi Wang, Lichao Ma,* Yifei Lu, Zhongzheng Li, Fuying Liang, JiZhai Cui, Wei Cheng, Fan Xu, Zhijin Hou, Yongfeng Mei, Xing Sheng, and Enming Song*

With the increasing demand for advanced biomedical technologies, there is a pressing need for flexible, integrated systems capable of simultaneously detecting and stimulating biological processes with high precision and reliability. In this study, an on-chip integrated flexible electronic system is successfully fabricated that combines both photoelectric detection and stimulation functionalities. This system integrates single-crystal silicon nanomembrane (Si-NM) photodiode array with micro-all-inorganic light-emitting diodes (µ-ILEDs), achieving comprehensive flexibility and complete encapsulation. The Si-NM photodiode exhibits broad responsivity across the visible light spectrum. Observed spatial response variations enable the detector array to accurately capture spatial information, precisely determining the position and direction of the light sources. Notably, the system incorporates an ultrathin thermally grown silicon dioxide (t-SiO$_2$) biofluid barrier. This barrier ensures stable leakage current in the device following 120 h of immersion in 90 °C PBS solution, guaranteeing long-term stability and reliability. Furthermore, this barrier effectively prevents the infiltration of toxic elements into surrounding tissues, ensuring the safety and biocompatibility of the implant. By leveraging advanced materials and manufacturing technologies, this system not only enhances the performance of optoelectronic devices but also expands their application scope in the biomedical field, opening new avenues for future biomedical research and clinical innovations.

1. Introduction

The integration of photodetectors and micro-all-inorganic light-emitting diodes (µ-ILEDs) represents a significant advancement in modern optoelectronic technology.[1] This integration facilitates the efficient detection and emission of light signals, finding extensive applications in diverse fields such as biomedicine, wearable devices, smart sensors, and flexible electronics.[1b,2] The photodiode, as a critical component, not only excels in photoelectric signal conversion but also enhances the versatility and adaptability of system.[3] While traditional silicon-based photodiodes offer advantages such as low cost and mature fabrication processes, they exhibit limitations in high performance applications.[4] Single-crystal silicon nanomembrane (Si-NM) photodiodes, an advanced optoelectronic device based on silicon materials, play a critical role in modern optoelectronics and semiconductor technology.[5] The ultrathin structure of Si-NM significantly enhances electron mobility and photoelectric

X. Wang, L. Ma, Y. Lu, Z. Li, F. Liang, J. Cui, Z. Hou, Y. Mei, E. Song
Institute of Optoelectronics & Innovation School of Future Information
Department of Materials Science
Shanghai Frontiers Science Research Base of Intelligent Optoelectronics and Perception
Fudan University
Shanghai 200438, China
E-mail: lichao_ma@fudan.edu.cn; sem@fudan.edu.cn
X. Wang, L. Ma, Y. Lu, Z. Li, F. Liang, J. Cui, Y. Mei, E. Song
International Institute for Intelligent Nanorobots and Nanosystems,
Neuromodulation and Brain-machine-interface Centre
Fudan University
Shanghai 200438, China

J. Cui, Y. Mei
Yiwu Research Institute of Fudan University
Yiwu, Zhejiang 322000, China
W. Cheng
Institute of Science and Technology for Brain-Inspired Intelligence
Fudan University
Shanghai 200438, China
F. Xu
Institute of Mechanics and Computational Engineering
Department of Aeronautics and Astronautics & College of Intelligent Robotics and Advanced Manufacturing
Fudan University
Shanghai 200433, China
Z. Hou
State Key Laboratory of Medical Neurobiology and MOE Frontiers Center for Brain Science
Fudan University
Shanghai 200433, China

ADVANCED
SCIENCE NEWS

www.advancedsciencenews.com

ADVANCED
MATERIALS
TECHNOLOGIES

www.advmattechnol.de

conversion efficiency. The quantum confinement effect at the nanoscale positively influences carrier behavior, improving device response speed and sensitivity.[6] Additionally, single-crystal silicon shows excellent stability, low cost, and well-established preparation methods, providing a robust foundation for large-scale production and practical applications.

In the traditional field of bioelectronic engineering, rigid electronic materials such as silicon wafers, due to their inherent rigidity and brittleness, struggle to conform perfectly to the curved surfaces of soft human tissues or skin.[7] This mechanical mismatch causes discomfort for patients and limits the comfort and safety of long-term wear or implantation. The advent of flexible technology has addressed these challenges by enabling the fabrication of electronic devices that match the flexibility of the human body.[8] Concurrently, through miniaturization design, these devices become more lightweight and compact, substantially enhancing user comfort and biocompatibility.[9] By controlling the dimensions of silicon materials at the nanometer scale, unique mechanical flexibility can be imparted, providing an opportunity to fabricate electronic devices on flexible substrates and ultimately achieving the construction of large-area flexible circuits and systems.[10] Numerous studies have highlighted the advantages and potential of Si-NM in applications such as biosensors and neural electronic interfaces.[11] For example, Song's research group developed a flexible, biocompatible multifunctional smart contact lens (P&T@DG) utilizing ultrathin single-crystal Si-NM (200 nm thick).[11a] Employing flexible transfer printing and micro-nano fabrication techniques, this device can rapidly and accurately detect intraocular pressure fluctuations and monitor ocular surface temperature, facilitating multidimensional auxiliary diagnosis of glaucoma. This progress is attributed to the development of flexible transfer technology, which allows for the precise and efficient transfer of functional materials like Si-NM from rigid substrates to flexible ones. The process maintains the electrical properties of Si-NM while endowing the devices with flexibility. Compared to direct growth methods on flexible substrates, flexible transfer technology typically gives exceptional film quality and uniformity.[12] By avoiding high-temperature processing on flexible substrates, this method prevents potential damage to the substrates, ensuring their integrity and performance.[12b]

The core of Si-NM transfer technology lies in utilizing specific process methods, such as chemical etching, laser lift-off, and mechanical exfoliation, to separate the Si-NM from its rigid substrate

X. Sheng
Department of Electronic Engineering
Beijing National Research Center for Information Science and Technology
Center for Flexible Electronics Technology
Tsinghua University
Beijing 100084, China
X. Sheng
IDG/McGovern Institute for Brain Research
Tsinghua University
Beijing 100084, China
E. Song
State Key Laboratory of Integrated Chips and Systems
Frontier Institute of Chip and System
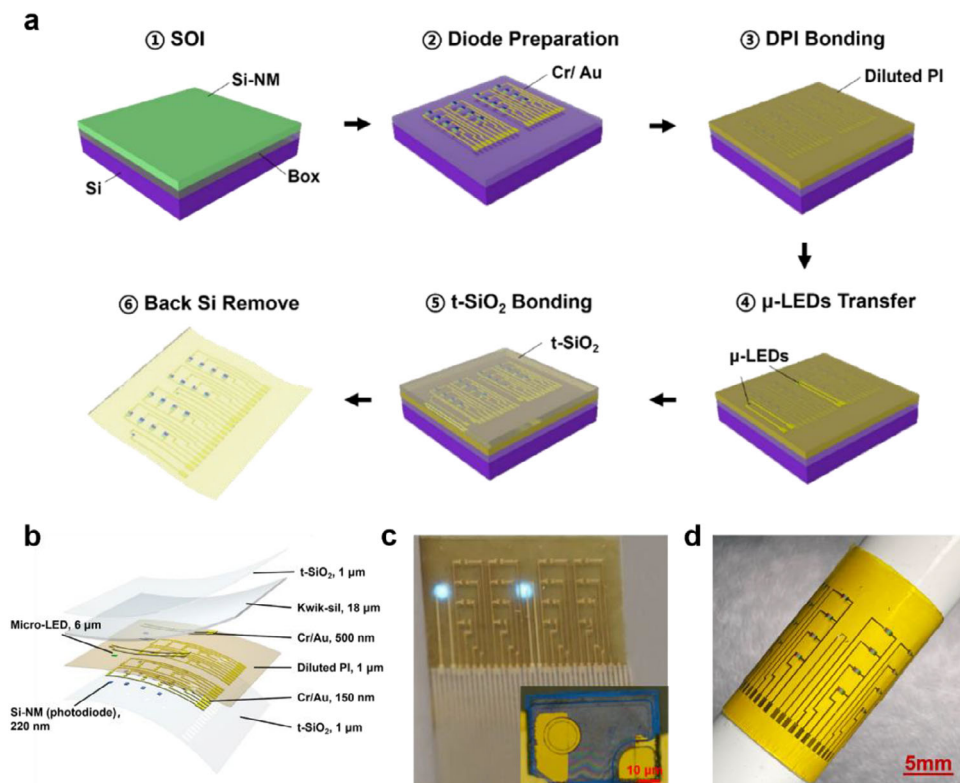Fudan University
Shanghai 200438, China

(e.g., silicon wafer) and transfer it intact onto a flexible substrate. This process requires precise control of parameters including temperature, pressure, and time to guarantee the integrity and electrical properties of the Si-NM unaffected.[11c] However, impurities are inevitably introduced during the transfer process, which may compromise the electronic transport characteristics and device performance.[13] This transfer method faces limitations in terms of efficiency and repeatability when applies to large-area film exceeding 5 cm × 5 cm.[14] In order to cope with these challenges, Rogers research group proposed an innovative strategy: fabricating the device on a silicon-on-insulator (SOI) structure, followed by peeling off the prepared Si-NM device along with the buried oxide layer from the rigid substrate.[15] This approach not only ensures the pristine photoelectric properties of the single-crystal Si-NM throughout the entire transfer process but also significantly elevates the reliability and consistency of the transfer.

Another key conundrum in the development of flexible electronic devices is the implementation of effective encapsulation barriers. These barriers play a crucial role in safeguarding the long-term isolation of internal components from the surrounding environment. Traditional encapsulation methods typically rely on a variety of organic and inorganic materials,[16] as well as metals and ceramics.[17] For instance, while polyimide (PI) and epoxy resins offer superior flexibility, they display relatively poor barrier properties.[18] Conversely, metals and ceramics provide robust physical protection but require thick and rigid enclosures, which limits their applicability to flexible and wearable devices.[19] To address this issue, researchers have explored the use of composite structures that combine different types of materials to achieve a balance between flexibility and protective performance. For example, alternating layers of organic polymers and inorganic oxides can be deposited on a flexible substrate to enhance barrier effects.[20] Despite some successes with this approach, pinholes and defects in the encapsulation layer can still allow environmental molecules and moistures to penetrate the device, leading to higher permeability and compromising long-term stability and reliability. A more novel and promising alternative is the utilization of the thermally grown silicon dioxide (t-SiO$_2$). Studies have demonstrated that the t-SiO$_2$ films with a thickness of 1 μm exhibit extremely low water vapor transmission rates, ranging from 10^{-6} to 10^{-8} g m^{-2} d^{-1} at 25 °C and 100% relative humidity.[21] This remarkable performance makes it an ideal candidate for biofluid barriers. The t-SiO$_2$ offers conspicuous chemical and thermal stability, assuring consistent performance across a wide temperature range. Moreover, t-SiO$_2$ has exceptionally high transmittance in the visible and near-infrared bands, typically exceeding 90%, which makes it particularly suitable for optical applications.[22]

In this study, we successfully fabricate an on-chip photodetector based on a SOI structure and integrate it with μ-ILEDs, forming an advanced system that combines photodetection and stimulation capabilities. To achieve overall flexibility and effective encapsulation, the prepared Si-NM device, along with the buried oxide layer, is carefully delaminated from the rigid substrate. The Si-NM photodetector demonstrates superior electrical and optical performance. Furthermore, the device manifests unparalleled mechanical deformation resistance, maintaining stable performance even after exceeding 1000 bending cycles. Notably, the thin t-SiO$_2$ film serves as an effective biological fluid

e00261 (2 of 10)

**ADVANCED
SCIENCE NEWS**

www.advancedsciencenews.com

**ADVANCED
MATERIALS
TECHNOLOGIES**

www.advmattechnol.de

Figure 1. a) Process flow for the optoelectronic integrated system involving photodiodes and μ-LEDs which are encapsulated by t-SiO$_2$ on a flexible substrate. (1) The fundamental structure of the SOI serves as the foundation, upon which devices are fabricated utilizing the Si-NM layer. (2) The photodiodes are fabricated by patterning the Si-NM using processes such as photolithography, thermal diffusion doping, and plasma etching. A bilayer of Cr (10 nm) and Au (150 nm) is subsequently deposited to form the top metal electrodes. (3) The diluted PI is applied as the device isolation layer through the spin-coating process. (4) The μ-LEDs are transferred onto the device surface, followed by the deposition of a Cr (20 nm)/Au (500 nm) bilayer as the metal electrodes. (5) An additional layer of t-SiO$_2$ is transferred to serve as the upper encapsulation layer of the system. (6) A flexible system is achieved by removing the bulk silicon from the backside via dry etching. b) Illustration of the optoelectronic integrated system encapsulated with t-SiO$_2$. c) An image of two μ-LEDs operating simultaneously on an integrated device. The inset presents the enlarged optical image of an individual LED. d) Optical image of the optoelectronic integrated system on a flexible substrate in a bent state (bending radius 10 mm).

barrier, enabling long-term stable implantation characteristics. This innovative design not only achieves efficient photoelectric conversion and precise light stimulation but also, owing to its excellent stability and biocompatibility, is well-suited for long-term in vivo applications as a reliable implant.

2. Results and Discussion

2.1. The Fabrication Process of a Flexible Integrated Photoelectric System That Combines Photodetection and Light-Emission Capabilities

The fabrication method encompasses the production of Si-NM photodiode arrays, the integration of these photodiodes with μ-LEDs, a comprehensive encapsulation strategy, and the realization of flexibility, as schematically illustrated in **Figure 1a** and Figures S1 and S2 (Supporting Information). An optical microscope image of the on-chip Si-NM photodiode array and an enlarged optical microscope image of a single P–N junction are presented in Figure S3 (Supporting Information). A detailed discussion of these processes is provided in the Experimental Section. The fabrication process includes doping, isolation, and metalliza-

tion steps to form isolated Si-NM photodiode arrays on a SOI substrate; Diluted polyimide (DPI) bonding, μ-LED transfer printing via stamp, and metal wiring of μ-LEDs enable the coupling of the Si-NM photodiode array with μ-LEDs; The transfer of an additional t-SiO$_2$ layer and the subsequent removal of the silicon substrate result in a flexible electronic device featuring double-sided t-SiO$_2$ encapsulation layers. An exploded-view schematic illustration of the key functional layers is depicted in Figure 1b. Figure 1c presents an image of two μ-LEDs operating simultaneously on an integrated device. Additionally, the inset depicts the enlarged optical image of an individual LED. An optical image (Figure 1d) shows the integration of Si-NM photodiode array with the μ-LED system on a flexible substrate in a bent state (with a bending radius of 10 mm), demonstrating that this electronic device enables to conform to surfaces of various shapes and sizes and particularly suitable for biomedical, wearable, and flexible electronics applications. Photodiodes are employed for efficient light signal detection, while μ-LEDs are utilized for light signal emission. The integration of these two components enables the system to perform both light detection and emission on a single platform, thereby significantly simplifying circuit design and enhancing the overall integration and reliability of the system.
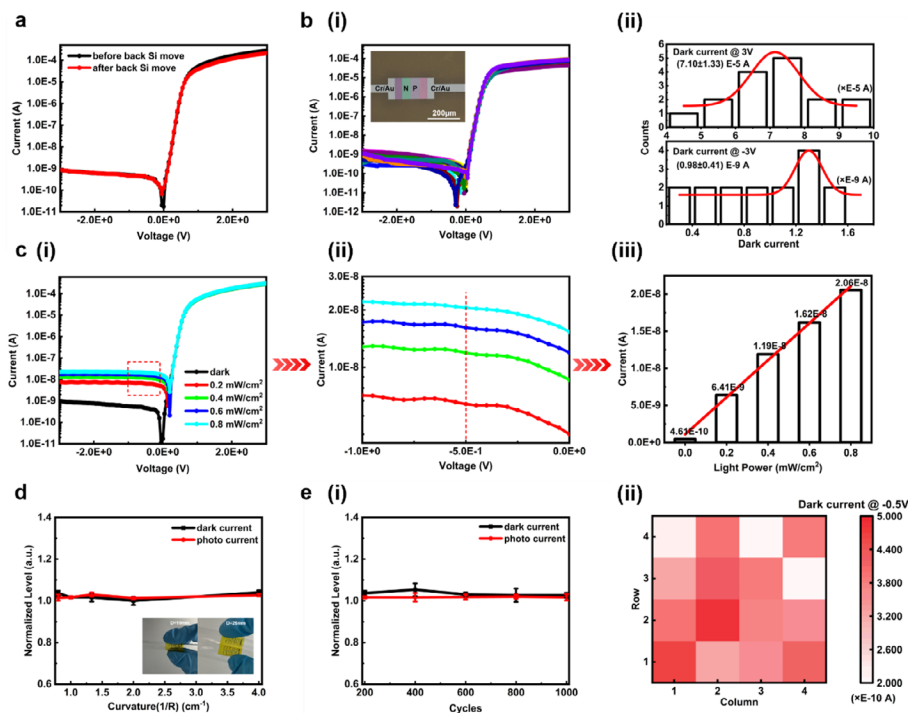
**ADVANCED
SCIENCE NEWS**

www.advancedsciencenews.com

**ADVANCED
MATERIALS
TECHNOLOGIES**

www.advmattechnol.de

Figure 2. a) *I–V* characteristic curves for the Si-NM photodetector before and after the removal of the backside bulk silicon. b-i) Dark and photocurrent of 16 photodiodes in the Si-NM photodetector array. Inset: optical image of a single device. (ii) the normal distribution statistics results on the dark currents at various voltages. c-i) Photodetector as a function of voltage under white light intensities of 0.2, 0.4, 0.6, and 0.8 mW cm^{-2}. (ii) *I–V* characteristic curves in the −1 to 0 V range (red box in (i)). iii) Photocurrent and dark current of the Si-NM photodetector as a function of white light power at a −0.5 V bias. d) Comparison variations in the normalized dark current and photocurrent level (0.4 mW cm^{-2}) at −0.5 V bias under different bending diameters (5, 10, 15, 20, 25 mm). Error bars represent the standard deviation derived from three replicate measurements. Inset: optical images of the device at bending diameters of 10 mm and 25 mm. e-i) Current variation levels during the bending cycle test with a diameter of 10 mm. Error bars represent the standard deviation derived from three replicate measurements. (ii) Dark currents at −0.5 V bias for 16 photodiodes in the Si-NM photodetector array after 1000 bending cycles.

2.2. Photoelectric Characteristics of the Flexible Integrated Photoelectric System

Following a series of meticulously designed and executed preparation steps, we successfully fabricated an array of Si-NM photodiodes. Optoelectronic devices must be equipped with outstanding electrical and optical performance as well as sustain stable operation in complex mechanical environments. In particular, ensuring that the photoelectric performance stays unaffected during the pursuit of flexibility and extensibility has emerged as a critical technical challenge. To address this challenge, we conduct comprehensive experimental research by comparing the current (*I*)–voltage (*V*) characteristic curves of Si-NM photodetector before and after removing the backside bulk silicon, as illustrated in **Figure 2a**. The results demonstrate that the dark current changes minimally, the photoelectric current response remains consistent, and the *I–V* characteristics are similar both before and after the removal of the back bulk silicon. These findings suggest that enhancing device flexibility does not significantly impact its photoelectric properties.

Subsequently, we investigate the uniformity of the flexible photodiode array. Figure 2b illustrates the dark *I–V* characteristic curves of the 16 photodiodes within the array, along with a statistical analysis of the normal distribution of dark currents at various voltages. The data clearly demonstrates a high degree of performance consistency among the photodiodes, indicating that the fabrication process for the array has been highly successful and yields no observable damage or defects. This conclusion is further corroborated by the optical image shown in the inset of Figure 2b–i. The turn-on voltage of the device is as low as 0.5 V, enabling the photodiode can operate at a reduced operating voltage. This feature significantly reduces energy consumption and enhances operational efficiency. The current switching ratio is on the order of 10^5, making sure that the on-state current is substantially higher than the off-state current. This characteristic guarantees high sensitivity and reliable signal detection.[23] The reverse bias current is on the order of 0.1 nA, demonstrating excellent dark current characteristics. This low reverse bias current not merely minimizes noise interference but improves the signal-to-noise ratio, allowing the photodiode to maintain high precision and stability even under low-light conditions.[24]

Light illumination exerts a significant influence on the electrical properties of silicon nanofilms, and its mechanism can be comprehensively analyzed from the following perspectives[25]: 1) When the energy of incident photons exceeds the bandgap energy of silicon, electron–hole pairs are generated, increasing the free carrier concentration; 2) Photogenerated carriers alter the charge distribution, reducing net charge density and narrowing the

**ADVANCED
SCIENCE NEWS**

www.advancedsciencenews.com

**ADVANCED
MATERIALS
TECHNOLOGIES**

www.advmattechnol.de

depletion region width; 3) The narrowing of the depletion region width results in a reduction of the Schottky barrier height, enhancing carrier transport properties; 4) The presence of photogenerated carriers induces photocurrent and alters the electrical characteristics of the device; 5) Illumination may also influence the surface states of silicon nanofilms, indirectly affecting the interface properties. To evaluate the electrical characteristics of the fabricated Si-NM photodiodes under different illumination conditions, we exposed them to white light with controlled intensity. The light source utilized in the experiment is precisely calibrated to warrant consistent light intensity. Figure 2c presents the *I–V* characteristic curves under dark conditions and varying light intensities. Under dark conditions, the device exhibits a dark current of 0.46 nA at a bias voltage of −0.5 V, indicating the presence of a small dark current even in the absence of illumination. This current is primarily attributed to defects, impurities, or intermediate-level trap states within the material.[26] The photocurrent increases and reaches saturation at low reverse bias under white light excitation. The primary cause of the increased photocurrent under low reverse bias is the expansion of the depletion region and the intensification of the built-in electric field.[27] These factors collectively enhance the efficient collection of photogenerated carriers, ultimately resulting in the saturation of the photocurrent. Under a bias of −0.5 V, the photocurrent shows a distinct linear growth trend with the increasing light intensity (Figure 2c-iii). Specifically, when the irradiation power is set to 0.2, 0.4, 0.6, and 0.8 mW cm^{-2}, the corresponding measured photocurrents are 6.41, 11.9, 16.2, and 20.6 nA, respectively. These results not only confirm the excellent linearity of the response of photodetectors to variations in light intensity but even highlight its consistent performance stability across a wide range of light intensities, from low to high.

Figure 2d illustrates the variations in normalized dark current and photocurrent (0.4 mW cm^{-2}) levels at a bias voltage of −0.5 V for bending diameters of 5, 10, 15, 20, and 25 mm. Through more than three repeated tests, the device performance sustains highly stable both before and after bending, irrespective of whether it is in dark conditions or under illumination. The current levels are on the order of 10^{-9} A, indicating remarkable mechanical flexibility and reliability. The inset images in Figure 2d show optical images of the diode array at bending diameters of 10 mm and 25 mm, respectively. Figure 2e shows the results obtained from the 10 mm diameter bending cycle. The reference value is established as the device current level at a −0.5 V bias prior to bending. The data demonstrate that, under both illuminated and non-illuminated conditions, as well as after multiple bending cycles, the device current is consistent with its performance before bending. After undergoing 1000 bending cycles, the 16 photodiodes in the array exhibit minimal dark current deviation at a −0.5 V bias, indicating that the array maintains stable performance even after repeated bending. The outstanding mechanical deformation resistance of Si-NM photodiodes ensures their long-term reliability and consistent performance across a wide range of application scenarios.

The absorption spectrum of Si-NM photodiodes on flexible substrates in the visible light range elucidates their wavelength-dependent light absorption characteristics. To achieve a more comprehensive understanding, we conducted an in-depth analysis of absorption performance of the device across the visible spectrum, as illustrated in **Figure 3a**. In the blue light region (450–495 nm), the photodiodes exhibit a relatively high absorption efficiency, primarily due to the significant photon absorption coefficient of Si-NM within this wavelength range. Additionally, the sub-nanometer thickness of the PN junction significantly minimizes surface recombination of photogenerated carriers, thereby enhancing the overall absorption performance in the blue light region. In the green light region (495–570 nm), the absorption efficiency decreases due to the lower absorption coefficient of the Si-NM compared to that in the blue light region. In the red light region (620–750 nm), the absorption efficiency further diminishes. This reduction is primarily caused by the insufficient thickness of the Si-NM (on the order of submicron) to effectively absorb long-wavelength photons, allowing partial penetration of red light and consequently reducing the absorption efficiency. Based on these findings, we employ the dry transfer method to transfer blue and green µ-LEDs and systematically compare their *I–V* characteristics (Figure 3b). It is abundantly clear that the *I–V* curves of both blue and green µ-LEDs exhibit flawless superposition, both prior to and following the transfer process. The turn-on voltages steadfastly maintain a constant level of 2.5 V, while the electrical performance demonstrates remarkable consistency. Using a blue µ-LED as the light source and placing it at various locations on the photodetector array (The response curves of the photodetector to varying intensities of blue light, as well as the corresponding current values at a bias voltage of −0.5 V, are illustrated in Figure S4, Supporting Information). By systematically varying the position of µ-LED, we are able to precisely control the distance between the light source and each detector, enabling a detailed investigation of the spatial distribution and variation in light response. Based on the *I–V* characteristic curve, we generated a light response map of the photodetector array (Figure 3c). This map clearly illustrates the current variations in each photodetector as the µ-LED is positioned at different locations. Specifically, when the µ-LED is placed at the edge or corner, the photocurrent response exhibits a pronounced gradient, with detectors closer to the light source showing stronger responses and those farther away demonstrating weaker responses. In the design of optical sensors, adjusting the position of the µ-LED can optimize the light sensing performance in specific regions to meet diverse application requirements.[28] When the µ-LED is centered, despite minor variations in response due to geometric differences, the overall photocurrent distribution across the array remains relatively uniform, demonstrating consistent light sensitivity. This configuration is particularly suitable for applications requiring uniform illumination, such as biomedical imaging or environmental monitoring, ensuring that all detectors receive light signals of consistent intensity, thereby enhancing data accuracy and reliability. The observed spatial variations in response enable the array to recognize spatial information, allowing for precise determination of the position and direction of the light source.

2.3. Stability and Biocompatibility of the Flexible Integrated Photoelectric System

Under physiological conditions, stability and biocompatibility are critical parameters for assessing the performance and safety of
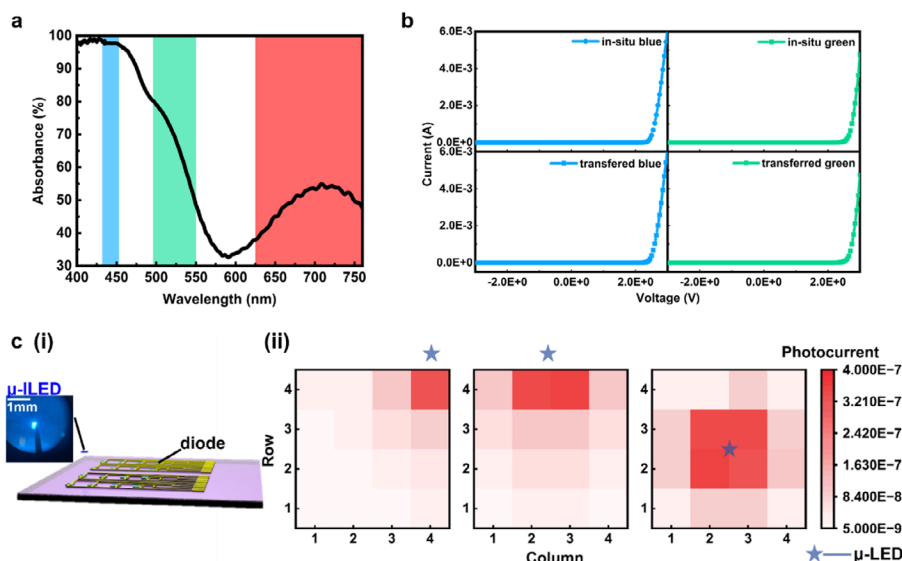
**ADVANCED
SCIENCE NEWS**

www.advancedsciencenews.com

**ADVANCED
MATERIALS
TECHNOLOGIES**

www.advmattechnol.de

Figure 3. a) Absorption spectrum of Si-NM photodetectors on flexible substrates in the visible light range. b) Comparison of $I-V$ characteristic curves of μ-LEDs before and after flexible transfer: the left two panels show blue LEDs, and the right two panels show green LEDs. c-i) Schematic illustration of placing a μ-LED at the upper right corner of the Si-NM photodetector array. (ii) Light response mapping of the μ-LED at various positions within the array.

biomedical devices. A significant advantage of this device is its comprehensive encapsulation achieved through the utilization of the SOI buried layer and an additional transferred SiO_2 layer. To validate the encapsulation performance, we conduct an accelerated aging experiment and leakage component analysis on the system encapsulated with t-SiO_2. Figure S5 (Supporting Information) unveils a schematic of the experimental setup designed to subject the device to accelerated immersion in a 90 °C PBS solution, employing a polydimethylsiloxane-based (PDMS) well structure to precisely confine the solution. **Figure** 4a reveals the test results for a 500 nm thick layer of t-SiO_2 immersed in the same rigorous conditions. The leakage current measurements obtained using the potentiostat reveal that the device maintains a leakage current below 2.5 nA after 120 h of immersion in PBS. Figure 4b illustrates the temperature-dependent measurements of hydrolysis rate of t-SiO_2 in PBS at pH of 7.4. The results demonstrate a strong linear correlation between the hydrolysis rate and $1/T$, consistent with Arrhenius scaling.[29] Data analysis reveals an apparent activation energy of $E_A = 1.32$ eV, corresponding to an exceptionally low thickness change rate at 37 °C ($\approx$0.04 nm d^{-1}).[30] These finding suggests that a 500 nm thick t-SiO_2 encapsulation layer can guarantee a minimum lifespan of 30 years for the encapsulated devices under physiological temperature conditions. In addition, the results of the leakage component analysis indicate that the 500 nm t-SiO_2 layer dissolves uniformly in the 90 °C PBS solution. Prior to complete dissolution, no leakage of Cr, Au, and Ga elements is observed within the device (Figure 4c). This indicates that our photonic integrated system exhibits promising potential for application as a stable implant.

Furthermore, cytotoxicity experiments validate the biocompatibility of the device, serving as a complementary assessment to the in vitro immersion tests conducted using ICP-OES measurements. White light and fluorescence microscopy images of

stained live (green) and dead (red) cells (mouse cardiac fibroblasts, L929) co-cultured with our photonic integrated device for 1 and 3 d are shown in Figure 4d. Figure 4e displays the relative viability of L929 cells assessed using a cell counting kit-8 (CCK-8) assay. A comparison between the experimental samples and the control samples (cells cultured without devices) demonstrates that there is no statistically significant difference in relative cell viability between these two groups ($P > 0.05$). This is consistent with the previous literature reports,[31] which indicate that flexible GaAs photodetectors with ultrathin thermally grown silicon dioxide layers can be used as chronic biomedical implants. Subsequently, we carry out in vivo experiments on the device. Figure 4f presents the experimental image of the device implanted in the cerebral cortex of a rat. The results reveal that, after 7 d of implantation, the $I-V$ characteristic curve of the Si-NM photodiode remains largely consistent with that prior to implantation (Figure 4g), thereby validating the excellent long-term implantability of the device. Furthermore, Figure 4h demonstrates that, following 7 d of implantation, the performance of the 16 photodiodes on the device exhibit high consistency, substantiating the stability of the device during this timeframe. It can therefore be concluded that the flexible integrated photoelectric system, which combines both light detection and emission capabilities, exhibits excellent stability and biocompatibility. These properties render it highly suitable for use as a reliable implantable device for long-term in vivo applications.

3. Conclusion

In summary, by integrating an on-chip Si-NM photodetector based on SOI architecture with μ-LEDs, and leveraging cutting-edge transfer techniques and advanced encapsulation processes, we have successfully engineered a flexible device that seamlessly combines photoelectric detection and stimulation capabilities.
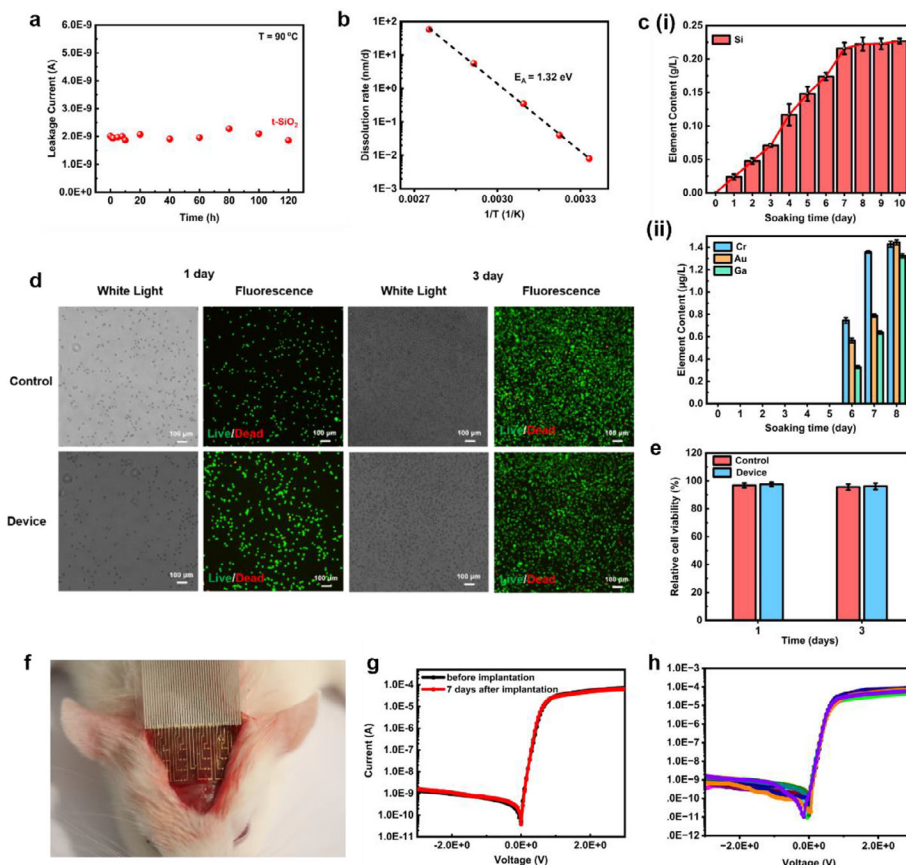
**ADVANCED
SCIENCE NEWS**

www.advancedsciencenews.com

**ADVANCED
MATERIALS
TECHNOLOGIES**

www.advmattechnol.de

Figure 4. The working stability and biocompatibility of the t-SiO$_2$ encapsulation system. a) The time-dependent current response of the photoelectric system immersed in a 90 °C PBS solution. b) Dissolution rate of t-SiO$_2$ in PBS at different temperatures at pH of 7.4. c) Concentrations of Si (i) and Cr, Au, Ga (ii) as a function of duration immersed in PBS solution (PH 7.4 at 90 °C). Error bars represent the standard deviation derived from three replicate measurements. d) White light and fluorescence microscopy images of live/dead-stained L929 cells cocultured with the device (bottom) and without devices (top) as control samples. e) Relative viability of L929 cells as a function of culture time (1 and 3 d), compared with control groups. Error bars represent the standard deviation derived from three replicate measurements. f) A photograph of the device implanted in the cerebral cortex of a rat. g) The I–V characteristic curve of the Si-NM photodiode measured before and after 7 d of implantation. h) Dark and photocurrent of 16 photodiodes in the Si-NM photodetector array after 7 d of implantation.

This innovative device boasts superior electrical and optical performance, along with exceptional resistance to mechanical deformation, enabling it to withstand over 1000 bending cycles. The observed spatial response variations enable the detector array to accurately capture spatial information, precisely determining the position and orientation of the light source. The incorporation of an ultrathin t-SiO$_2$ biofluid barrier guarantees stable leakage current even after 120 h of immersion in 90 °C PBS solution. Furthermore, this barrier effectively prevents the leaching of toxic elements into surrounding tissues, ensuring the safety and reliability of the device. This innovative achievement holds significant potential for future biomedical research and clinical applications and is poised to become a viable candidate for long-term stable implants.

4. Experimental Section

Fabrication Details: Cleaning Protocol: The preparation process for the Si-NM photodiode array based on the SOI wafer involved a meticulously designed cleaning protocol to ensure that the Si-NM, which grown along

the (001) crystal direction with an initial bulk doping concentration of 10^{15} cm^{-3} and a corresponding surface resistivity of 13.3 Ω cm, was free from organic particles, natural oxide layers, and ionic pollutants. The detailed steps were as follows:

1) Ultrasonic clean sequentially with acetone/alcohol/deionized water for 2 min each;
2) RCA 1: Immerse the sample in SC-1 solution (deionized water: 30% H$_2$O$_2$: 29% NH$_4$OH = 5:1:1) at 70 °C for 10 min to remove organic contaminants;
3) Buffered oxide etch (BOE, deionized water: HF = 6:1) for 30 s to eliminate natural oxide layers formed on the surface of silicon nanofilms;
4) RCA 2: Immerse the sample in SC-2 solution (deionized water: 30% H$_2$O$_2$: 39% HCl = 5:1:1) at 75 °C for 10 min to remove ionic pollutants;
5) Thoroughly ultrasonic clean the sample with deionized water to remove any residual solution and subsequently blow dry with a nitrogen gun.

Manufacturing Process of Si-NM Photodiode Array: The detailed fabrication process for Si-NM photodiode arrays was as follows:

1) Prepare clean samples with the specified dimensions: Cut the n-type SOI wafer (with a 220 nm thick top Si-NM, a 1 μm thick buried

**ADVANCED
SCIENCE NEWS**

www.advancedsciencenews.com

**ADVANCED
MATERIALS
TECHNOLOGIES**

www.advmattechnol.de

oxide layer, and a 200 µm thick initial silicon substrate) into 2 cm × 2 cm pieces. Thoroughly clean, followed by blow-drying to ensure clean surfaces.

2) Thermal diffusion doping: 1) Deposit a 600 nm SiO_2 mask on the Si-NM surface using plasma-enhanced chemical vapor deposition (PECVD) equipment at a deposition temperature of 350 °C for 8 min; 2) Define the etching window using photolithography technology. Apply positive photoresist S1813 in hard contact mode with the following parameters: spin-coat at 4000 rpm for 30 s, pre-bake at 115 °C for 90 s, expose for 7 s, post-bake at 115 °C for 3 min, and develop using rx3080 developer for 35 s. Blow dry the sample with nitrogen gas; 3) Reactive ion etching (RIE) system and BOE solution to define the P-type thermal diffusion doping region of the Si-NM device. The parameters were as follows: pressure 50 mTorr, gas flow rate 40 sccm CF_4/1 sccm O_2, RF power 100 W for 5 min. Subsequently, immerse the sample in BOE solution for 2 min to achieve hydrophobicity in the etched window; 4) Remove the photoresist and blow dry the sample; 5) Perform thermal diffusion doping using Boron solid source. Pre-diffusion was conducted in a N_2 atmosphere with a flow rate of 1 L min^{-1} at 960 °C for 15 min, followed by redistribution in at 1100 °C for 35 min in an ambient atmosphere. Remove the mask using HF. After soaking the doped SOI wafer in 49% HF for 30 s, the Si-NM surface became completely hydrophobic.

3) Silicon nanofilm device isolation: 1) Define the device area using photolithography technology. Apply positive photoresist S1813 in hard contact mode and expose for 7 s; 2) Isolate the device region using RIE technology. The RIE parameters were as follows: pressure 100 mTorr, gas flow rate 15 sccm SF_6/3 sccm O_2, and RF power 50 W for 140 s; 3) Remove the photoresist and blow off any residue.

4) Metallization: 1) Deposit the electrode material (Cr/Au) using magnetron sputtering equipment. The Ar gas flow rate was 19 sccm, and the pressure was 2 mTorr. Sputter Cr at 130 W for 24 s (resulting in a 10 nm thickness) and Au at 135 W for 150 s (resulting in a 150 nm thickness); (2) Define the metallization area using photolithography with positive photoresist S1813; 3) Perform wet etching of Au and Cr using their respective etchants; 4) Remove the photoresist and blow off any residue; 5) Conduct rapid thermal annealing in N_2 atmosphere at 340 °C for 2 min.

Fabrication of Si-NM Photodetectors Coupled with µ-LED: The µ-LEDs are provided by the Xing Sheng Research Group at Tsinghua University. The fabrication of thin-film µ-LEDs encompasses several fundamental steps, including epitaxial growth, microdevice fabrication, release from the source wafer, and transfer as well as printing onto the target substrate or circuit. Blue, green, and violet LEDs are generally grown on sapphire substrates with a GaN buffer layer. The GaN buffer layer is decomposed via laser lift-off, enabling the separation of µ-LEDs from the sapphire substrate through gentle mechanical force applied at 70 °C. Subsequently, the samples are immersed in a dilute ammonia solution (1:5 aqueous solution) for approximately 30 min to eliminate residual gallium. Finally, the thin-film µ-LEDs are separated from the temporary release tape by heating them to 120 °C. The detailed fabrication process is referred to the prior publications of the Xing Sheng Research Group.[32] Then, the integration of µ-LEDs with the photodiode array is as follows:

1) Apply DPI (PI: dimethyl acetamide (DMAC) = 2.5:1) as the adhesive layer. Spin coat DPI on SOI wafer containing Si-NM photodetectors at 5000 rpm for 30 s, followed by a soft bake at 110 °C for 3 min and 30 s to achieve a thickness of approximately 1 µm.

2) Transfer the µ-LED to the DPI substrate using a prepared PDMS stamp. Prepare the transfer stamp by curing PDMS (base: curing agent = 4:1) at 60 °C for 24 h, cutting it into the desired shape, and bonding it to a glass substrate. Lift the µ-LED from the temporary substrate and transfer it to the designated device position. Place the sample on a hot plate at 110 °C, then gently release the PDMS stamp at 90 s. Soft bake the sample at 150 °C for 3 min.

3) Metal wiring of µ-LEDs: Deposit Cr/Au electrodes using magnetron sputtering technology. Define the metal electrode region using photolithography and metal etching solutions.

Encapsulation Strategies with t-SiO$_2$ Barriers: The buried oxide layer in SOI wafer, t-SiO$_2$, served as the back-surface biofluid barrier after device was fabricated on the top silicon layer and the bulk silicon was removed. The second transferred t-SiO$_2$ layer as the front-surface biofluid barrier.

A 1 µm thick PI coating and a separate adhesive layer (Kwik-Sil, World Precision Instruments) were spin-coated onto the second t-SiO$_2$ wafer. Inductively coupled plasma-reactive ion etching (ICP-RIE, 50 mTorr of SF_6/O_2, 40/3 sccm, with RF power of 1200 W) and RIE (50 mTorr of SF_6/O_2, 15/3 sccm, with RF power of 100 W) were employed to remove the bulk silicon, exposing a 1 µm thick t-SiO$_2$ layer as the biofluid barrier on the PI substrate, which was laminated on a temporary glass plate. A similar method was used to remove the bulk silicon from the t-SiO$_2$ wafer. Peeling off the entire sample from the glass substrate resulted in a flexible electronic device encapsulated by top and bottom t-SiO$_2$ layers.

Characterization: The I–V characteristics under dark and white light with varying intensities were measured using a probe station and a semiconductor parameter analyzer (Keithley 4200A). The leakage current in PBS solution was evaluated using a potentiostat (CHI600E). The concentration of Si, Cr, Au, and Ga were quantified using inductively coupled plasma optical emission spectrometry (ICP-OES, Agilent 7800). The variations in the thickness of t-SiO$_2$ during immersion in PBS solutions at varying temperatures were quantified using ellipsometry.

Cytotoxicity Evaluation: Following sterilization via ultraviolet irradiation, the photoelectric integrated device was co-cultured with L929 cells (Procell Life Science & Technology Co. Ltd.) in a constant temperature incubator at 37 °C for 24 and 72 h, respectively. The cultured cells were stained using the calcein acetoxymethyl/propidium iodide (AM/PI) double-stain kit (BB-4126, BestBio) and incubated at room temperature for 15 min. Fluorescence microscope was employed to capture images of the stained live and dead cells. To evaluate relative cell viability, the co-cultured cells were incubated in culture medium supplemented with 10% CCK-8 solution (IV08-100, Invigentech) for 2 h at 37 °C. The absorbance at 450 nm, measured using a microplate reader, was used to quantify the relative viability of the cells.

In Vivo Experiment of Animal Models: All the animal experiments were approved by the Animal Welfare and Ethics Committee of the Experimental Animal Center of Fudan University (Approval Number: 202504001S) and were conducted under its supervision. All in vivo experiments were performed on 6-week-old male rats. Rats were induced into inhalation anesthesia using a 0.5 mL min^{-1} air flow containing 4% isoflurane. Subsequently, the rats were transferred to a stereotactic apparatus and maintained under anesthesia via a built-in mask. The ventilation rate of isoflurane was adjusted according to the respiratory condition of the rats. The skin on the top of the rat's head was carefully incised using ophthalmic scissors to expose the skull. A small burr hole was then drilled in the skull to access the cerebral cortex region. Finally, the device was gently attached to the surface of the cerebral cortex.

Supporting Information

Supporting Information is available from the Wiley Online Library or from the author.

Acknowledgements

Conflict of Interest

The authors declare no conflict of interest.

Data Availability Statement

The data that support the findings of this study are available from the corresponding author upon reasonable request.

Keywords

[1] a) S. Chang, J. H. Koo, J. Yoo, M. S. Kim, M. K. Choi, D.-H. Kim, Y. M. Song, *Chem. Rev.* **2024**, *124*, 768; b) K. Liao, Y. Lian, M. Yu, Z. Du, T. Dai, Y. Wang, H. Yan, S. Wang, C. Lu, C. T. Chan, R. Zhu, D. Di, X. Hu, Q. Gong, *Nat. Photonics* **2025**, *19*, 358; c) Y.-Q. Bie, G. Grosso, M. Heuck, M. M. Furchi, Y. Cao, J. Zheng, D. Bunandar, E. Navarro-Moratalla, L. Zhou, D. K. Efetov, T. Taniguchi, K. Watanabe, J. Kong, D. Englund, P. Jarillo-Herrero, *Nat. Nanotechnol.* **2017**, *12*, 1124.

[2] W. Wu, L. Li, Z. Li, J. Sun, L. Wang, *Adv. Mater.* **2023**, *35*, 2304596.

[3] a) T. Huang, S. Lin, J. Zou, Z. Wang, Y. Zhong, J. Li, R. Wang, Z. Wang, K. St Luce, R. Kim, J. Cui, H. Wang, Q. Li, M. Xu, S. Shen, X. Zhang, *ACS Appl. Mater. Interfaces* **2024**, *17*, 1861; b) W. Song, J. Kang, K. Elkhouly, S. Hamdad, X. Zhang, M. I. Pintor Monroy, A. B. Siddik, P. Carolan, S. Subramaniam, Y. Kuang, F. D. Roose, E. Vandenplas, N. Chandrasekaran, J. H. Kim, R. Gehlhaar, S.-J. Kim, J. Lee, J. Genoe, *ACS Nano* **2024**, *18*, 35520.

[4] a) H. Dou, L. Liu, J. Gou, C. Li, X. Yang, J. Chen, J. Han, H. Zhou, H. Yu, Z. Wu, J. Wang, *ACS Photonics* **2024**, *11*, 3688; b) T. Bu, X. Duan, C. Liu, W. Su, X. Hong, R. Hong, Y. Liu, Z. Fan, X. Zou, L. Liao, X. Liu, *Adv. Funct. Mater.* **2023**, *33*, 2305490.

[5] a) Y. Huang, Y. Cui, H. Deng, J. Wang, R. Hong, S. Hu, H. Hou, Y. Dong, H. Wang, J. Chen, L. Li, Y. Xie, P. Sun, X. Fu, L. Yin, W. Xiong, S.-H. Shi, M. Luo, S. Wang, X. Li, X. Sheng, *Nat. Biomed. Eng.* **2023**, *7*, 486; b) B. Wu, Z. Zhang, Z. Zheng, T. Cai, C. You, C. Liu, X. Li, Y. Wang, J. Wang, H. Li, E. Song, J. Cui, G. Huang, Y. Mei, *Adv. Mater.* **2023**, *35*, 2306715.

[6] C. Pan, Y. Tong, H. Qian, A. V. Krasavin, J. Li, J. Zhu, Y. Zhang, B. Cui, Z. Li, C. Wu, L. Liu, L. Li, X. Guo, A. V. Zayats, L. Tong, P. Wang, *Nat. Commun.* **2024**, *15*, 2840.

[7] a) S.-H. Sunwoo, S. I. Han, C. S. Park, J. H. Kim, J. S. Georgiou, S.-P. Lee, D.-H. Kim, T. Hyeon, *Nat. Rev. Bioeng.* **2024**, *2*, 8; b) Y. Zhao, B. Wang, J. Tan, H. Yin, R. Huang, J. Zhu, S. Lin, Y. Zhou, D. Jelinek, Z. Sun, K. Youssef, L. Voisin, A. Horrillo, K. Zhang, B. M. Wu, H. A. Coller, D. C. Lu, Q. Pei, S. Emaminejad, *Science* **2022**, *378*, 1222.

[8] I. Uguz, D. Ohayon, S. Yilmaz, S. Griggs, R. Sheelamanthula, J. D. Fabbri, I. McCulloch, S. Inal, K. L. Shepard, *Sci. Adv.* **2024**, *10*, adi9710.

[9] a) S. Nam, G. D. Cha, S. H. Sunwoo, J. H. Jeong, H. Kang, O. K. Park, K.-Y. Lee, S. Oh, T. Hyeon, S. H. Choi, S.-P. Lee, D.-H. Kim, *Adv. Mater.*

2024, *36*, 2404101; b) Y. Huang, H. Li, T. Hu, J. Li, C. K. Yiu, J. Zhou, J. Li, X. Huang, K. Yao, X. Qiu, Y. Zhou, D. Li, B. Zhang, R. Shi, Y. Liu, T. H. Wong, M. Wu, H. Jia, Z. Gao, Z. Zhang, J. He, M. Zheng, E. Song, L. Wang, C. Xu, X. Yu, *Nano Lett.* **2022**, *22*, 5944.

[10] A. K. Katiyar, B. J. Kim, G. Lee, Y. Kim, J. S. Kim, J. M. Kim, S. Nam, J. Lee, H. Kim, J.-H. Ahn, *Sci. Adv.* **2024**, *10*, adg7200.

[11] a) Y. Shao, B. Hu, X. Liu, Z. Ni, Y. Shu, X. Zhang, J. Shen, L. Liang, L. Zhou, J. Liu, X. Li, J. Zhang, L. Ma, Z. Di, Y. Mei, R. Li, Y. Bi, E. Song, *Biosens. Bioelectron.* **2025**, *267*, 116786; b) Y. Jiang, X. Li, B. Liu, J. Yi, Y. Fang, F. Shi, X. Gao, E. Sudzilovsky, R. Parameswaran, K. Koehler, V. Nair, J. Yue, K. Guo, Y. Fang, H.-M. Tsai, G. Freyermuth, R. C. S. Wong, C.-M. Kao, C.-T. Chen, A. W. Nicholls, X. Wu, G. M. G. Shepherd, B. Tian, *Nat. Biomed. Eng.* **2018**, *2*, 508; c) B. Hu, D. Xu, Y. Shao, Z. Nie, P. Liu, J. Li, L. Zhou, P. Wang, N. Huang, J. Liu, Y. Lu, Z. Wu, B. Wang, Y. Mei, M. Han, R. Li, E. Song, *Sci. Adv.* **2024**, *10*, eadp8804.

[12] a) Q. Xu, M. Jia, P. Zhou, Y. Zhang, W. Guo, S. Zhao, H. Zeng, J. Zhang, M. Yan, S. Jiang, K. Zhou, D. Zhang, C. Bowen, *Adv. Funct. Mater.* **2024**, *35*, 2414211; b) Y. Shin, S. Hong, Y. C. Hur, C. Lim, K. Do, J. H. Kim, D.-H. Kim, S. Lee, *Nat. Mater.* **2024**, *23*, 1411.

[13] A. Mondal, C. Biswas, S. Park, W. Cha, S.-H. Kang, M. Yoon, S. H. Choi, K. K. Kim, Y. H. Lee, *Nat. Nanotechnol.* **2024**, *19*, 34.

[14] C. Wang, C. Linghu, S. Nie, C. Li, Q. Lei, X. Tao, Y. Zeng, Y. Du, S. Zhang, K. Yu, H. Jin, W. Chen, J. Song, *Sci. Adv.* **2020**, *6*, abb2393.

[15] H. Fang, J. Zhao, K. J. Yu, E. Song, A. B. Farimani, C.-H. Chiang, X. Jin, Y. Xue, D. Xu, W. Du, K. J. Seo, Y. Zhong, Z. Yang, S. M. Won, G. Fang, S. W. Choi, S. Chaudhuri, Y. Huang, M. A. Alam, J. Viventi, N. R. Aluru, J. A. Rogers, *Proc. Natl. Acad. Sci. USA* **2016**, *113*, 11682.

[16] a) N. T. Kalyani, S. Dhoble, *Renewable Sustainable Energy Rev.* **2015**, *44*, 319; b) X. Xie, L. Rieth, S. Merugu, P. Tathireddy, F. Solzbacher, *Appl. Phys. Lett.* **2012**, *101*, 093702.

[17] a) K. A. Peterson, K. D. Patel, C. K. Ho, S. B. Rohde, C. D. Nordquist, C. A. Walker, B. D. Wroblewski, M. Okandan, *Int. J. Appl. Ceram. Technol.* **2005**, *2*, 345; b) C. S. Mestais, G. Charvet, F. Sauter-Starace, M. Foerster, D. Ratel, A. L. Benabid, *IEEE Trans. Neural Syst. Rehabil.* **2014**, *23*, 10.

[18] a) M. Sang, K. Kim, J. Shin, K. J. Yu, *Adv. Sci.* **2022**, *9*, 2202980; b) C. Zhao, C. Park, S. E. Root, Z. Bao, *Nat. Rev. Bioeng.* **2024**, *2*, 671.

[19] E. Song, J. Li, J. A. Rogers, *APL Mater.* **2019**, *7*, 050902.

[20] a) S.-W. Seo, E. Jung, H. Chae, S. M. Cho, *Org. Electron.* **2012**, *13*, 2436; b) D. Wen, R. Yuan, F. Yang, R. Chen, *Dalton Trans.* **2024**, *53*, 14656.

[21] E. Song, J. Li, S. M. Won, W. Bai, J. A. Rogers, *Nat. Mater.* **2020**, *19*, 590.

[22] G. Li, E. Song, G. Huang, R. Pan, Q. Guo, F. Ma, B. Zhou, Z. Di, Y. Mei, *Small* **2018**, *14*, 1802985.

[23] a) W. Yang, T. Chen, L. Xie, Y. Yu, M. Long, L. Xu, *Carbon Neutralization* **2024**, *3*, 904; b) C. Zhang, S. Peng, J. Han, C. Li, H. Zhou, H. Yu, J. Gou, C. Chen, Y. Jiang, J. Wang, *Adv. Funct. Mater.* **2023**, *33*, 2302466.

[24] O. J. Sandberg, C. Kaiser, S. Zeiske, N. Zarrabi, S. Gielen, W. Maes, K. Vandewal, P. Meredith, A. Armin, *Nat. Photonics* **2023**, *17*, 368.

[25] a) A. K. Katiyar, B. J. Kim, G. Lee, Y. Kim, J. S. Kim, J. M. Kim, S. Nam, J. Lee, H. Kim, J.-H. Ahn, *Sci. Adv.* **2024**, *10*, adg7200; b) W. Liu, J. Shi, L. Zhang, A. Han, S. Huang, X. Li, J. Peng, Y. Yang, Y. Gao, J. Yu, K. Jiang, X. Yang, Z. Li, W. Zhao, J. Du, X. Song, J. Yin, J. Wang, Y. Yu, Q. Shi, Z. Ma, H. Zhang, J. Ling, L. Xu, J. Kang, F. Xu, J. Liu, H. Liu, Y. Xie, F. Meng, et al., *Nat. Energy* **2022**, *7*, 427.

[26] J. Kublitski, A. Hofacker, B. K. Boroujeni, J. Benduhn, V. C. Nikolis, C. Kaiser, D. Spoltore, H. Kleemann, A. Fischer, F. Ellinger, K. Vandewal, K. Leo, *Nat. Commun.* **2021**, *12*, 551

[27] L. Qi, W. Tang, X. Weng, K. Wu, Y. Cen, Y. Sun, S. Zhou, Z. Li, X. Wu, C. Kang, D. Zhao, S. Dai, Y. Xie, H. Liang, W. Zhang, Y.-J. Zeng, S. Ruan, *Adv. Funct. Mater.* **2024**, *34*, 2315991.

[28] a) B. Ouyang, J. Wang, G. Zeng, J. Yan, Y. Zhou, X. Jiang, B. Shao, Y. Chai, *Nat. Electron.* **2024**, *7*, 705; b) J. Liu, P. Liu, T. Shi, M. Ke,

**ADVANCED
SCIENCE NEWS**

www.advancedsciencenews.com

**ADVANCED
MATERIALS
TECHNOLOGIES**

www.advmattechnol.de

K. Xiong, Y. Liu, L. Chen, L. Zhang, X. Liang, H. Li, S. Lu, X. Lan, G. Niu, J. Zhang, P. Fei, L. Gao, J. Tang, *Nat. Commun.* **2023**, *14*, 5352.

[29] E. Song, C.-H. Chiang, R. Li, X. Jin, J. Zhao, M. Hill, Y. Xia, L. Li, Y. Huang, S. M. Won, K. J. Yu, X. Sheng, H. Fang, M. A. Alam, Y. Huang, J. Viventi, J.-K. Chang, J. A. Rogers, *Proc. Natl. Acad. Sci. USA* **2019**, *116*, 15398.

[30] E. Song, J. Li, S. M. Won, W. Bai, J. A. Rogers, *Nat. Mater.* **2020**, *19*, 590.

[31] N. Hong, D.-M. Geum, T. S. Kim, S.-Y. Ahn, J.-H. Han, D. Jung, G. Ryu, S. Kim, K. J. Yu, W. J. Choi, *Adv. Photonics Res.* **2021**, *2*, 2000051.

[32] a) J. Chen, H. Ding, X. Sheng, *J. Inf. Disp.* **2024**, *25*, 1; b) C. Liu, X. Sheng, *Mater. Today* **2024**, 279, https://doi.org/10.1016/B978-0-443-18845-9.00012-0.